RESEARCH ARTICLE | APRIL 02 2024

Copper effects on the microstructures and deformation mechanisms of CoCrFeNi high entropy alloys FREE

Special Collection: Era of Entropy: Synthesis, Structure, Properties, and Applications of High-Entropy Materials

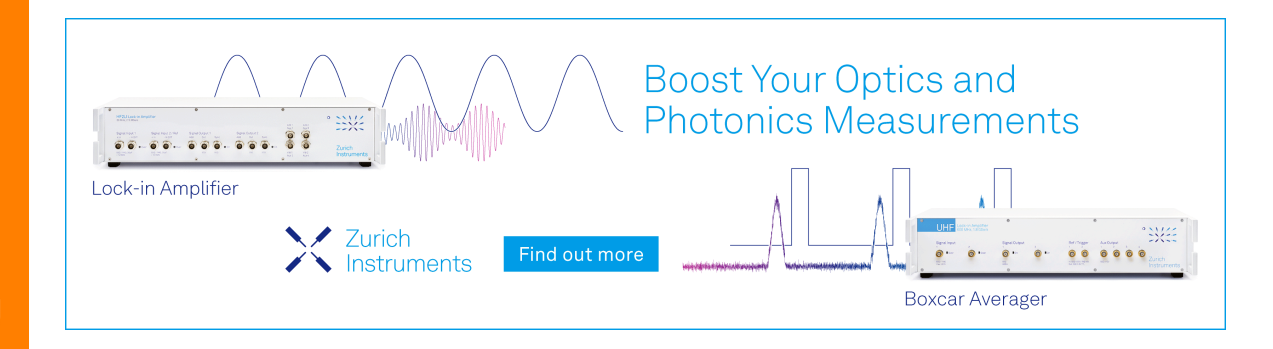
Lia Amalia [®] ; Yongkang Li [®] ; Hongbin Bei [®] ; Yan Chen [®] ; Dunji Yu; Ke An [®] ; Zongyang Lyu; Peter K. Liaw [®] ; Yanwen Zhang; Qingqing Ding ■ [®] ; Yanfei Gao ■ [®]



Appl. Phys. Lett. 124, 141901 (2024) https://doi.org/10.1063/5.0201647









Copper effects on the microstructures and deformation mechanisms of CoCrFeNi high entropy alloys

Cite as: Appl. Phys. Lett. **124**, 141901 (2024); doi: 10.1063/5.0201647 Submitted: 31 January 2024 · Accepted: 24 March 2024 · Published Online: 2 April 2024







Lia Amalia,^{1,2} (D) Yongkang Li,³ (D) Hongbin Bei,³ (D) Yan Chen,⁴ (D) Dunji Yu,⁴ Ke An,⁴ (D) Zongyang Lyu,¹ Peter K. Liaw,¹ (D) Yanwen Zhang,^{1,5} Qingqing Ding,^{3,a)} (D) and Yanfei Gao^{1,a)} (D)

AFFILIATIONS

- Department of Materials Science and Engineering, University of Tennessee, Knoxville, Tennessee 37996, USA
- ² Teknik Material dan Metalurgi, Institut Teknologi Kalimantan, Balikpapan 76127, Indonesia
- ³School of Materials Science and Engineering, Zhejiang University, Hangzhou, 310027 Zhejiang, China
- 4 Neutron Scattering Division, Oak Ridge National Laboratory, Oak Ridge, Tennessee 38731, USA

Note: This paper is part of the APL Special Collection on Era of Entropy: Synthesis, Structure, Properties, and Applications of High Entropy Materials.

^{a)}Authors to whom correspondence should be addressed: qq_ding@zju.edu.cn and ygao7@utk.edu

ABSTRACT

In situ neutron diffraction experiments have been performed to investigate the deformation mechanisms on CoCrFeNi high entropy alloys (HEAs) with various amounts of doped Cu. Lattice strain evolution and diffraction peak analysis were used to derive the stacking fault probability, stacking fault energy, and dislocation densities. Such diffraction analyses indirectly uncovered that a lower degree of Cu doping retained the twinning behavior in undoped CoCrFeNi HEAs, while increasing the Cu content increased the Cu clusterings which suppressed twinning and exhibited prominent dislocation strengthening. These results agree with direct observations by transmission electron microscopy.

Published under an exclusive license by AIP Publishing. https://doi.org/10.1063/5.0201647

High entropy alloys (HEAs) which were independently developed by Yeh and Cantor have uncovered novel deformation mechanisms, contrasting typical traditional alloys in the past 20 years. Previous studies revealed that HEAs possess unique features such as short-range ordering (SRO),³ large lattice distortion,⁴ transformation-induced plasticity (TRIP),5 twinning-induced plasticity (TWIP),6 strong and dense nanoprecipitates,7 and compositional waves, which led to enhancement of mechanical properties. Although these interesting mechanisms have previously been revealed, it needs to be pointed out that they operate in vastly different alloy systems, making it elusive to quantitatively assess and compare these mechanisms. It is more desirable to have one alloy system that has the potential to be developed into a wide range of microstructural features, deformation mechanisms, and desirable properties so that quantitative comparisons could be done, similar to existing conventional alloy systems such as nickel-based superalloys and stainless steels. 10

At the early stage of research on HEAs, CoCrFeMnNi was one of the pioneering alloy systems that was studied for its mechanical behavior. CoCrFeMnNi revealed interesting mechanical behavior, especially at cryogenic temperatures, where both ductility and ultimate strength were increased up to 60% elongation to failure and 1000 MPa, respectively. 11 At cryogenic temperature, twinning is activated from approximately 8% of true strain, with nanoscale twin size and micrometer-scale spacing, which act as boundaries for dislocation motion, providing the dynamic Hall-Petch effect.¹¹ At room temperature, the ultimate strength decreased to 460 MPa with elongation to failure of around 45%. 11 At an earlier stage of deformation, slip occurs on {111} planes by the planar glide of $1/2\langle 110 \rangle$ and then splits into $1/6\langle 112 \rangle$ Shockley partial dislocation. At further stages of deformation, around 15%-20% of straining, the partial dislocations are activated on multiple-slip systems, increasing the dislocation density. Toward the last stage of deformation, twinnings are finally formed. 11,11

⁵Energy and Environment Science & Technology, Idaho National Laboratory, Idaho Falls, Idaho 83415, USA

Tuning the element and chemical composition of HEAs has been shown to enhance the mechanical behavior of CrCoNi-based HEAs.8 By comparing CrCoFeNiPd and CrCoFeNiMn to CrCoFeNi, it was found that Pd addition increased the solid solution strengthening due to lattice size and shear modulus mismatch between CrCoFeNiPd and CrCoFeNi. Element clusterings leading to compositional waves were also reported to increase the obstacle-hardening effect. Incorporating nanoprecipitates by element tuning has also been reported to increase the strength of HEAs.7 A small addition of Ti and Cu to Al_{0.3}CoCrFeNi was reported to form L1₂ coherent precipitates and increase the strength to 1100 MPa. 13 Cu clusters also act as nucleation sites for L12 precipitates and contribute to the increased strength. The interaction of dislocation and precipitate was observed to be the bowing mechanism, leading to enhanced ductility. It was reported that higher strengthening was observed in the sample with smaller L1₂ particles. L2₁ precipitates were also observed to populate the grain boundaries, which could lead to grain boundary strengthening.¹³ Even though the effect of different compositions of alloying elements in high entropy alloys has been studied, it is rarely done within the same alloy system and to explicate the evolution of microstructure, mechanical properties, and other properties of interest caused by fine element tuning.14

Cu addition to CoCrFeNi-based HEA was reported to improve wear resistance, high-temperature hardness, high-temperature hardness, and corrosion resistance, they have also been studied for semisolid state processing. A simulation study revealed that CoCrCuFeNi has the largest stair-rod and Hirth dislocations density compared to CoCrFeNi and CoCrFeNiMn, acting as obstacles for dislocation. Cu clusterings were observed in previous studies of CoCrFeNi-xCu, but their role in mechanical properties has not been

fully investigated.^{28,29} Despite the aforementioned simulation and experimental studies, a systematic study of the compositional effect of Cu doping and the resulting microstructural tunability is still lacking, especially the roles played by possible nanoclusters, stacking faults, twinning, and their interactions are not clear.

In this study, we investigate the effect of increasing Cu content to CoCrFeNi (CoCrFeNi-xCu, x = 1, 3, and 5) by utilizing *in situ* neutron diffraction experiment. The specimens were prepared using arc melter, homogenized at 1100 °C for 8 h, rolled with 86% reduction, and annealed at 1050 °C for 30 min. Scanning electron microscopy (SEM) equipped with energy-dispersive spectroscopy (EDS), together with transmission electron microscopy (TEM), has been used for microstructural characterization. TEM studies were conducted to observe the microstructural change after the tension test. TEM samples were taken from both the undeformed samples and the gauge region. After grinding until around 50 μm thickness, the samples were electrochemically polished using twin-jet polishing with 5 vol. % perchloric acid-95 vol. % ethanol solution.

Figures 1(a)–1(c) show SEM images of the as-fabricated CoCrFeNi-1Cu, CoCrFeNi-3Cu, and CoCrFeNi-5Cu, respectively, showing all samples having similar grain sizes of around 70 μ m. EDS element maps on CoCrFeNi-1Cu and CoCrFeNi-5Cu in Figs. 1(d) and 1(e), respectively. Both CoCrFeNi-1Cu and CoCrFeNi-5Cu show the clusterings of Cu. However, the Cu cluster size in CoCrFeNi-1Cu is noticeably smaller compared to those in CoCrFeNi-5Cu. Many studies of the CoCrCuFeNi alloy system reported Cu clusterings, which sometimes could be identified in the x-ray diffraction pattern, overlapping with the FCC matrix diffraction pattern. 18,22 Consequently, our focus of this work is placed on the connection between microstructural

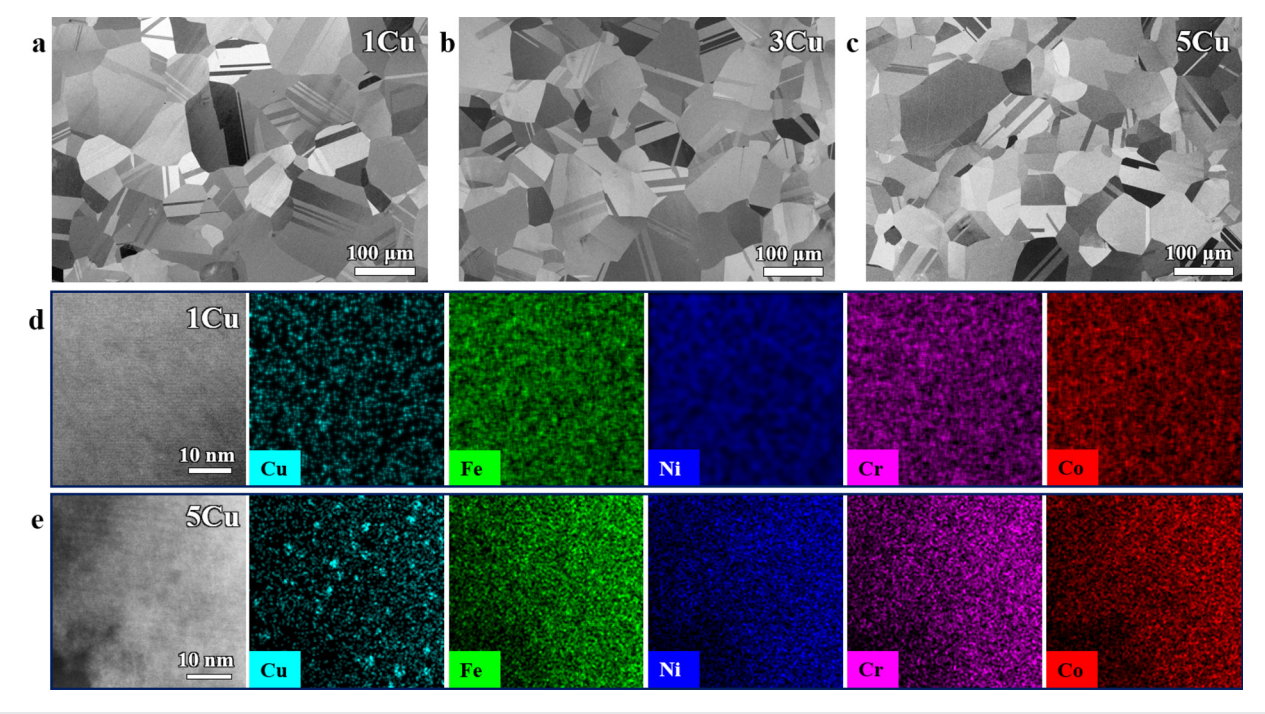


FIG. 1. Scanning electron microscope (SEM) images of the (a) CoCrFeNi-1Cu, (b) CoCrFeNi-3Cu, and (c) CoCrFeNi-5Cu microstructures showing similar grain sizes (around 70 μm) and EDS element map images of (d) CoCrFeNi-1Cu showing smaller sized clusterings of Cu and (e) CoCrFeNi-5Cu showing larger sized Cu clusters.

change (i.e., from homogenous solution without Cu doping to nanoclusters with 1Cu, 3Cu, and 5Cu) and mechanical properties (i.e., from twinning/stacking fault behavior in CoCrFeNi to possible nanocluster-strengthening mechanisms in 1Cu, 3Cu, and 5Cu).

Utilizing in situ neutron diffraction techniques allows for observation and quantitative investigation of microstructural change during tensile loading, such as peak intensity, peak width, d-spacing, and individual lattice strain, making the observation of interesting mechanical behavior possible.³⁰ In this work, in situ neutron diffraction studies were performed in the Spallation Neutron Source (SNS) and Oak Ridge National Laboratory (ORNL), using the engineering diffractometer in the VULCAN beamline.31 There are two detector banks at ±90° to the incident beam for the diffraction data collection, which corresponds to the neutron diffraction in the loading direction with the vector of diffraction parallel to the applied load [Bank 1 (Q_{II}) Detector] and transverse direction with the vector of diffraction perpendicular to the applied load [Bank 2 (Q1) Detector] [Fig. 2(a)]. The samples were machined as per the requirement of VULCAN room temperature tension 3-mm dog bone plate sample (gauge size: $15 \times 2.6 \times 3 \text{ mm}^3$). The specimens were loaded in tension until fracture with a strain rate of 2×10^{-4} s⁻¹, which is a relatively slow strain rate to allow a sufficient neutron penetration to the sample.

The obtained diffraction data were chopped into 180-second intervals. GSAS software was used to conduct the full-pattern Rietveld refinement to observe the lattice parameter changes and phase fractions during loading. The data were also analyzed using single peak fitting by the VDRIVE software to obtain the hkl-specific behavior of the sample.³² The lattice-specific strain (ε_{hkl}) was obtained by calculating the ratio of the difference of lattice spacing of the specific orientation (d_{hkl}) to the orientation-specific lattice spacing prior to loading ($d_{0,hkl}$), as shown in the following equation:

$$\varepsilon_{hkl} = \frac{d_{hkl} - d_{0,hkl}}{d_{0,hkl}}. (1)$$

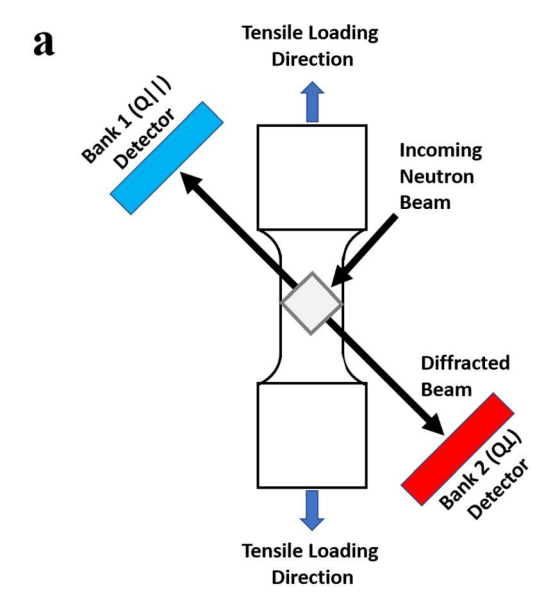
The stacking fault energy (SFE) is calculated with Reed and Schramm's relationship shown in Eq. (2), 33,34 where a_0 is the lattice parameter (nm), P_{sf} is the stacking fault probability (SFP), $\left\langle \epsilon_{50}^2 \right\rangle_{111}$ is the mean square strain, and C_{11} , C_{12} , and C_{44} are the single-crystal elastic constants (SCECs). SFP was evaluated by Eq. (3) from the peak shift caused by stacking fault, which was caused by the difference in lattice strains of {111} and {222} grains in FCC, while $\frac{1}{0.0517}$ was derived from reflection quantity of (111) and (222) orientation. Mean square strain, $\left\langle \epsilon_{50}^2 \right\rangle_{111}$, was calculated using the integral breadth method with pseudo-Voigt convolution [Eq. (4)], 36

$$SFE = \frac{6.6a_0}{\pi\sqrt{3}} \left(\frac{2c_{44}}{c_{11} - c_{12}} \right)^{-0.37} \frac{\left\langle c_{50}^2 \right\rangle_{111}}{P_{sf}} \left(\frac{c_{44} + c_{11} - c_{12}}{3} \right), \quad (2)$$

$$P_{sf} = \frac{1}{0.0517} \left(\varepsilon_{\{222\}} - \varepsilon_{\{111\}} \right), \tag{3}$$

$$\left\langle \varepsilon_{50}^{2}\right\rangle ^{1/2}=2\pi^{1/2}\beta_{G}\frac{d_{hkl}}{2}.$$
 (4)

The dislocation density was obtained from the modified Williamson–Hall peak broadening analysis [Eq. (5)], 37,38 where $\Delta K = -K(\Delta d/d)$ and K = 1/d, with d the d-spacing (nm) and Δd the



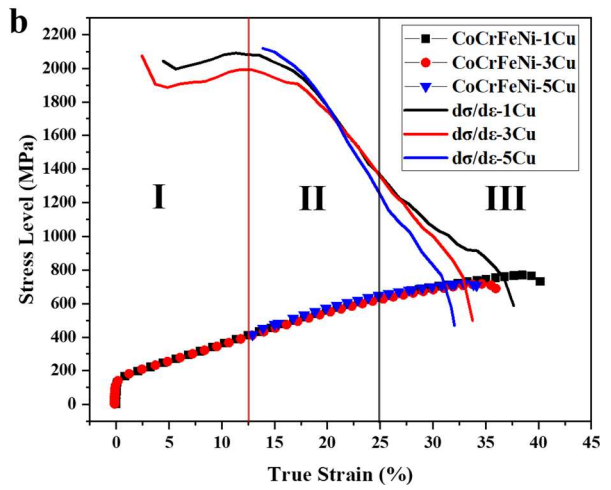


FIG. 2. (a) Schematic drawing of the experimental setup at Vulcan beamline, SNS, and ORNL. (b) True stress vs true strain overlapping with the work hardening rate $(d\sigma/d\epsilon)$ of CoCrFeNi-1Cu, CoCrFeNi-3Cu, and CoCrFeNi-5Cu, showing three different regions of deformation behavior.

peak broadening in the full-width at half maximum (FWHM) (nm). D is the grain size, A is a constant that depends on the effective outer cutoff radius of dislocation, b is Burger's vector of the dislocation ($b = \sqrt{2}a_0/2$), ρ is the dislocation density, and the last term refers to a noninterpreted higher-order term. C can be calculated using Eq. (6), which depends on C_{h00} and q, where their values are dependent on the dislocation type, the centering of the crystal, and the ratio of C_{12}/C_{44} , with C_{h00} calculated using ANIZC software. Dislocation density can be obtained by plotting $(\Delta K)^2$ vs K^2C of the (hkl) reflections, where the slope of linear regression is equivalent to $(\pi A^2 b^2/2)\rho$. The value of A needs to be determined using an initial value of dislocation density. In this study, we use the published value of dislocation density of CoCrFeNi in Ref. 40, 6.3×10^{14} m⁻², which makes the A value in our

case to be 0.429. The initial value of dislocation density was chosen because of the similar sample initial condition,

$$(\Delta K)^2 = (0.9/D)^2 + (\pi A^2 b^2) \rho(K^2 C) + O(K^2 C)^2,$$
 (5)

$$C = C_{h00} \left(1 - q \frac{h^2 k^2 + h^2 l^2 + k^2 l^2}{\left(h^2 + k^2 + l^2 \right)^2} \right).$$
 (6)

Figure 2(b) shows the true stress–strain curves and the work-hardening behaviors for CoCrFeNi-1Cu, CoCrFeNi-3Cu, and CoCrFeNi-5Cu. Due to the diffraction apparatus problem during testing, only half of the CoCrFeNi-5Cu data could be acquired; therefore, we could not obtain information on CoCrFeNi-5Cu during elastic deformation. All samples have similar yield strengths, which are 140 and 142 MPa for CoCrFeNi-1Cu and CoCrFeNi-3Cu, respectively. The ultimate tensile strengths for CoCrFeNi-1Cu, CoCrFeNi-3Cu, and CoCrFeNi-5Cu are 770, 717, and 719 MPa, respectively. The elongations to failure are 40%, 35%, and 34% for CoCrFeNi-1Cu, CoCrFeNi-3Cu, and CoCrFeNi-5Cu, respectively. The addition of copper is observed to not change the yield strength and only slightly reduced the ultimate tensile strength and elongation to failure. However, as will be shown shortly, the deformation mechanisms are radically different in these different alloys.

Based on Considère's necking criterion, when the strain hardening rate is equal to the stress in the uniaxial tensile stress-strain curve $(d\sigma/d\varepsilon = \sigma)$, necking is predicted to occur.⁴¹ As can be observed from Fig. 2(b), the necking occurred approximately at 759 MPa and 36.6% strain in CoCrFeNi-1Cu, 709 MPa and 33% strain in CoCrFeNi-3Cu, and 710 MPa and 31% strain in CoCrFeNi-5Cu. For CoCrFeNi-1Cu, the work hardening rate increased at Stage I and then decreased at Stage II. The decreasing rate slows down slightly toward the end, which is, thus, denoted as Stage III after 25% of strain. Meanwhile, the work hardening rate of CoCrFeNi-3Cu and CoCrFeNi-5Cu increased at Stage I but continued to decrease from Stage II until failure occurred. However, even when the addition of copper slightly reduced the elongation to failure and ultimate tensile strength, the mechanical behavior of CoCrFeNi-3Cu and CoCrFeNi-5Cu could still keep up with CoCrFeNi-1Cu. It compels us to look closer at the microstructural behavior of these alloys to explain the differences in deformation

Figures 3(a) and 3(b) show the measured diffraction patterns collected during the tensile loading for CoCrFeNi-1Cu and CoCrFeNi-3Cu. Both samples show only one phase during loading, which is the face-centered cubic (FCC) phase. Figures 3(c) and 3(d) show the lattice strain evolution of CoCrFeNi-1Cu and CoCrFeNi-3Cu obtained from the single peak fitting analysis. Two deformation stages could be observed from the slope of these lattice strains, which are the elastic deformation and plastic deformation. Elastic deformation occurs below the yield point (around 140 MPa), where all grain orientation is shown to have a linear relationship between the applied stress and the corresponding lattice strain. The plastic deformation behavior occurs after the yield point, where there are nonlinear relationship between the applied stress and the corresponding lattice strain.

For cubic materials, the anisotropy of the grain orientation could be characterized by the cubic elastic anisotropy factor, A_{hkl} [Eq. (7)], where h, k, and l are the Miller indices of the grains. The elastic strain of a specific grain orientation diffracted from the loading direction and transversal direction can be predicted using Eq. (8). With that, the

modulus of elasticity of a specific grain (E_{hkl}) could be calculated using Eq. (9), ⁴²

$$A_{hkl} = \frac{h^2 k^2 + k^2 l^2 + h^2 l^2}{\left(h^2 + k^2 + l^2\right)^2},\tag{7}$$

$$\frac{\varepsilon_{hkl,LD}}{\sigma} = S_{11} - 2[S_{11} - S_{12} - 0.5S_{44}]A_{hkl},\tag{8}$$

$$E_{hkl} = \frac{\sigma}{\varepsilon_{hkl}},\tag{9}$$

where S_{11} , S_{12} , and S_{44} are elastic compliance of the material obtained from the Kroner's self-consistent model. The calculated values are summarized in Tables I and II. Figures 3(c) and 3(d) show the {200} grains have the lowest elastic modulus, with {311} grains shown to be the second lowest, and then the other grains, {220}, {111}, and {222}, have the higher elastic modulus, which is consistent with the calculated E_{hkl} in Table II, cubic structure's elastic anisotropy factor, and other reported data. 43,44

During the plastic deformation, the applied load is distributed among the grains where softer grain families such as {220} transfer the load to the harder grain families, in this case {200} grains. Generally, both CoCrFeNi-1Cu and CoCrFeNi-3Cu follow this trend. However, some differences are noticeable. In FCC crystalline materials, the change in Bragg scattering positions in {111} and {222} could occur if stacking faults are formed; otherwise, they would have the same value. ⁴⁵ Figure 3(e) shows the difference of {111} and {222} in loading direction in CoCrFeNi-1Cu starting from 25% true strain, which we do not see in CoCrFeNi-3Cu, indicating stacking faults forming in CoCrFeNi-1Cu but not in CoCrFeNi-3Cu. Figure 3(f) shows the last stage of the work hardening rate evolution during tensile loading, showing CoCrFeNi-1Cu having a larger work hardening rate compared to CoCrFeNi-3Cu starting at a true strain of 25%. Coincidentally, as shown in Fig. 3(g), the stacking fault probability of CoCrFeNi-1Cu started to increase from around 1×10^{-4} to 3.317×10^{-3} . Meanwhile, the stacking fault probability of CoCrFeNi-3Cu is negligible since there are barely any differences in {111} and {222} lattice strains. Stacking fault probability can also be defined as the stacking fault formation frequency along the {111} plane in the fcc structure. Stacking fault interspacing is defined as the space between formed stacking faults, with a larger value indicating fewer stacking faults were formed. The average value of interspacing between formed stacking faults (L_{sf}) could be estimated using stacking fault probability and the d-spacing of {111} grain [Eq. (10)],⁴

$$L_{sf} = \frac{d_{111}}{P_{sf}}. (10)$$

Figure 3(h) shows the evolution of stacking fault interspacing with increasing strain. During elastic deformation, the L_{sf} of CoCrFeNi-1Cu reached 368 nm. The stacking fault interspacing continued to decrease with increasing strain levels where CoCrFeNi-1Cu reached saturation in L_{sf} value of around 62 nm. Note that reported stronger materials such as Co-Cr-Mo alloy⁴⁷ and Fe₄₀Mn₂₀Cr₁₅Co₂₀Si₅ (Ref. 46) had around 10 nm of L_{sf} after being heavily deformed. Since the stacking fault probability of CoCrFeNi-3Cu is negligible, we do not see clear evolution of stacking fault interspacing. The decrease in interspacing of stacking fault is correlated with the increased fault density as the material continues to deform until it breaks. The stacking fault hardening phenomenon has

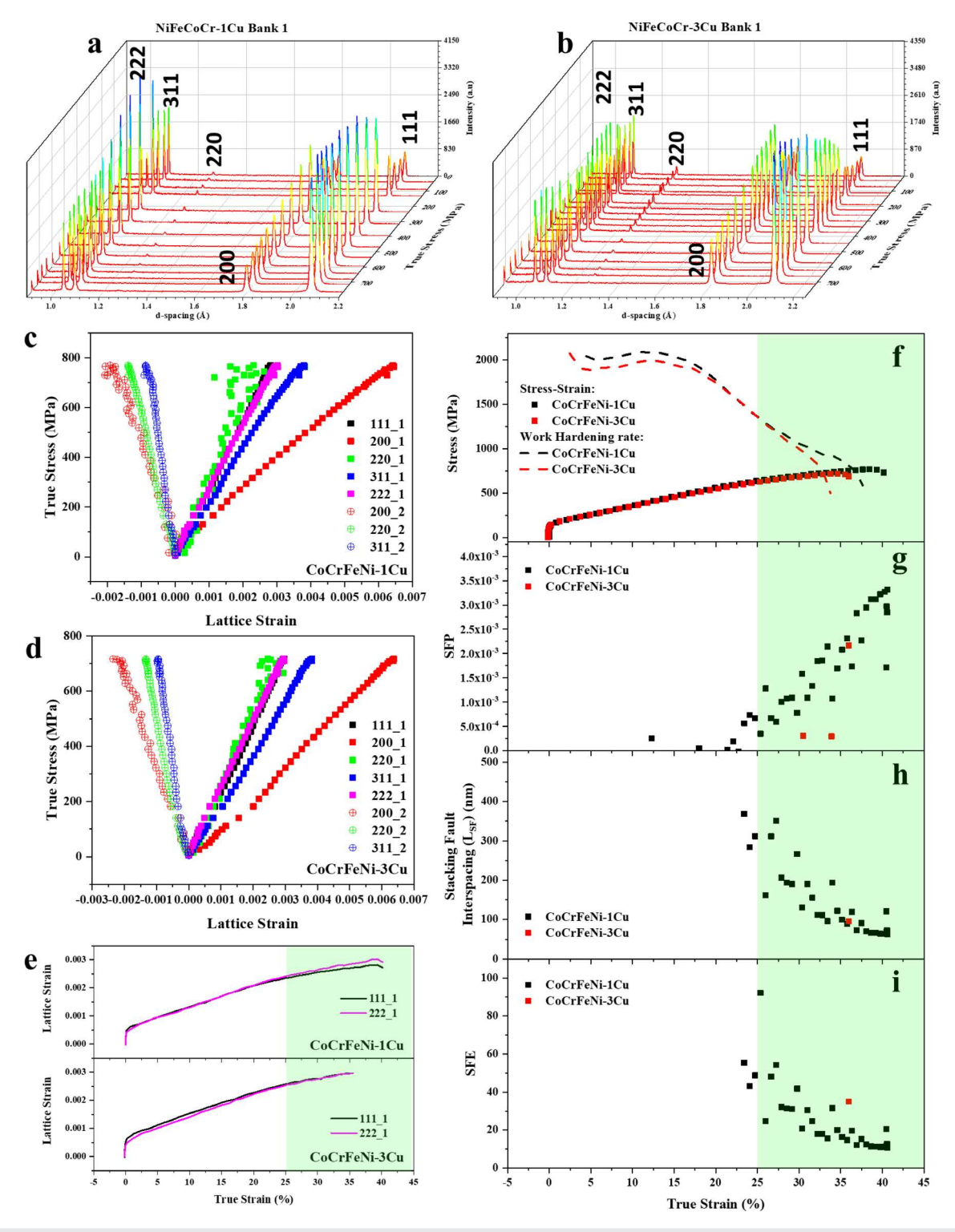


FIG. 3. The measured diffraction patterns upon tensile loading, collected at bank 1 (corresponding to loading direction) for (a) CoCrFeNi-1Cu and (b) CoCrFeNi-3Cu. The evolution of lattice strains in loading (bank 1) and transversal direction (bank 2) of (c) CoCrFeNi-1Cu and (d) CoCrFeNi-3Cu. (e) The lattice strain difference between {111} and {222} in CoCrFeNi-3Cu, indicating stacking fault formation. Higher (f) work hardening rate and (g) stacking fault probability, with lower (h) stacking fault interspacing and (i) stacking fault energy of CoCrFeNi-1Cu starting from 25% of strain as compared to CoCrFeNi-3Cu.

TABLE I. Calculated elastic constants.

	S ₁₁	$0^{-2} \frac{S_{12}}{GPa}$	S ₄₄	C ₁₁	C ₁₂ GPa	C ₄₄
CoCrFeNi-1Cu	0.716	-0.267	1.197	250.61	148.88	83.54
CoCrFeNi-3Cu	0.965	-0.401	1.094	253.42	180.18	91.40

TABLE II. Calculated elastic moduli with respect to specific grain orientations.

Grain orientation	111	200	220	311	222		
A_{hkl}	0.33	0	0.25	0.16	0.33		
	Calculated E_{hkl} along the loading direction (LD) (GPa)						
CoCrFeNi-1Cu	217.50	139.64	190.89	167.96	217.50		
CoCrFeNi-3Cu	238.67	103.66	180.05	141.32	238.67		

also been reported where it was experimentally observed that the increase in stacking fault interspacing corresponded to the delay of decrease in macroscopic strain hardening during plastic deformation, and the collapse of fault interspacing enabled strain hardening in $Fe_{38.5}Mn_{20}Cr_{15}Co_{20}Si_5Cu_{1.5}.^{48}$

Stacking fault energy is indicative of how easily a perfect dislocation splits into two partial dislocations. The range of SFE values has been used to indicate the deformation mechanism in various metals and also in high-entropy alloys. The SFE of less than 20 mJ/m² is reported in materials with phase transformation during loading, SFE between 20 and 45 mJ/m² typically deform by twinning, while SFE

beyond 45 mJ/m² deform by slip. 10,34,49 The stacking fault energy (SFE) of CoCrFeNi-1Cu and CoCrFeNi-3Cu is presented in Fig. 3(i). In CoCrFeNi-3Cu, the lattice strain of {222} grain never surpasses the lattice strain of {111} grain, until a few data points near the end of tensile loading, which explains why there is only one visible SFE in Fig. 3(i). In CoCrFeNi-1Cu, the SFE value is around 50 mJ/m² at around 25% of true strain and then gradually decreases to the value of 30–10 mJ/m² until the sample breaks. The average SFE of CoCrFeNi-1Cu is around 37 mJ/m². The evolution of SFE with increasing strain levels could be correlated with the changes in the deformation substructure.³⁴ TEM study on CoCrFeNi fabricated with high-pressure torsion reported the change of microstructure with the observation of nanoband, twinning, nanoband interactions, and nanoband-twin interactions with the increasing deformation level.⁵⁰ Hence, the *in situ* neutron diffraction patterns during deformation which captured the microstructural changes during deformation could provide us with parameters related to faulting, such as SFP, Lsf, and SFE, and their changes at each level of strain. Therefore, in the case of CoCrFeNi-1Cu, the increase in the work hardening rate at stage III, as seen in Fig. 2(b), is caused by the formation of twins, causing the dynamic Hall-Petch effect, consistent with the TEM evidence in Fig. 4(b) and literature.11

The dislocation density of CoCrFeNi-1Cu and CoCrFeNi-3Cu in common edge ($\langle 111 \rangle \{110\}$ type) and screw ($\langle 111 \rangle$ type) dislocation system at a true strain of 1%, 5%, 12%, 15%, 20%, 25%, 30%, and 35% is presented in Fig. 4(a) and summarized in Table III. The value of dislocation density of CoCrFeNi-3Cu shows minor differences as compared to CoCrFeNi-1Cu. There are also minor differences between edge and screw dislocations in both CoCrFeNi-1Cu and CoCrFeNi-3Cu. Figure 4(c) shows the microstructure image using TEM on CoCrFeNi-5Cu after the tensile test. The TEM image of highly

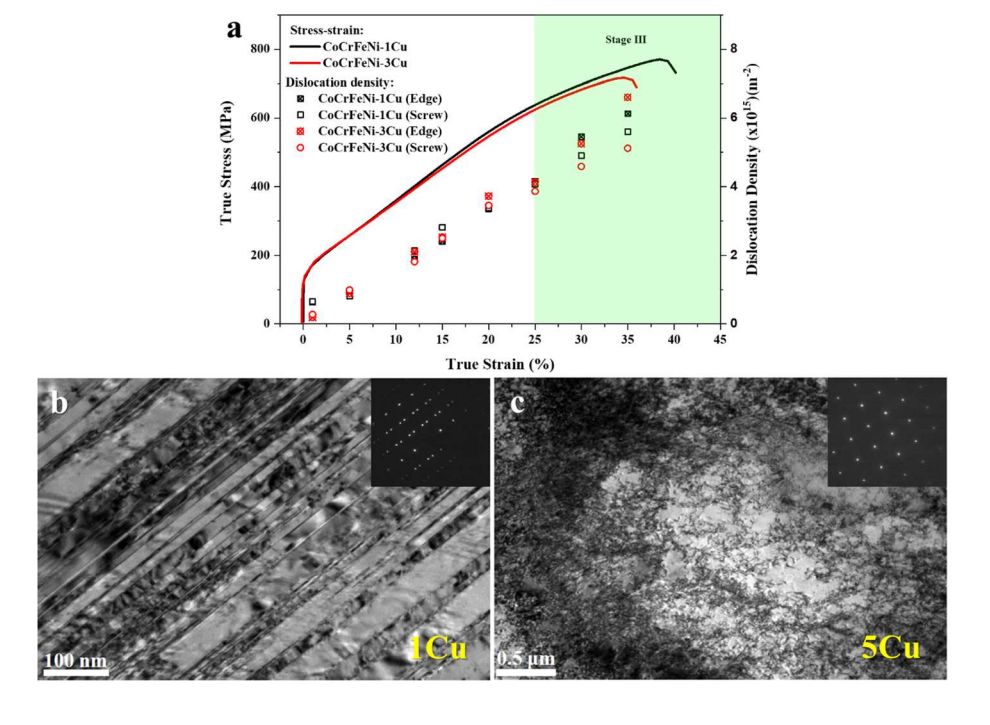


FIG. 4. (a) Dislocation density of CoCrFeNi-1Cu and CoCrFeNi-3Cu, with TEM images of (b) CoCrFeNi-1Cu showing twinnings and (c) CoCrFeNi-5Cu showing dislocation forests. Both images were taken near the end of the stress–strain curves in Fig. 2.

TABLE III. Slopes of the linear regression from the modified Williamson–Hall plot and dislocation densities of CoCrFeNi-1Cu and CoCrFeNi-3Cu at several strain levels, obtained from the modified Williamson–Hall peak broadening analysis.

		Slope (×10 ⁻⁴)				Dislocation density (×10 ¹⁵) (m ⁻²)			
True strain (%)	CoCrFeNi-1Cu		CoCrFeNi-3Cu		CoCrFeNi-1Cu		CoCrFeNi-3Cu		
	Edge	Screw	Edge	Screw	Edge	Screw	Edge	Screw	
1	0.117	0.121	0.035	0.051	0.628	0.653	0.187	0.276	
5	0.158	0.150	0.166	0.184	0.849	0.808	0.890	0.989	
12	0.353	0.399	0.393	0.339	1.891	2.139	2.104	1.816	
15	0.449	0.526	0.474	0.467	2.407	2.818	2.533	2.500	
20	0.626	0.631	0.696	0.646	3.346	3.372	3.719	3.450	
25	0.778	0.761	0.775	0.724	4.156	4.065	4.131	3.861	
30	1.021	0.919	0.985	0.861	5.449	4.906	5.250	4.588	
35	1.149	1.050	1.238	0.959	6.128	5.599	6.603	5.118	

deformed CoCrFeNi-5Cu shows many dislocations were formed after tensile loading, where the density of dislocation agrees with the calculated dislocation density listed in Table III. This goes to show that although CoCrFeNi-3Cu did not form twinnings, it formed enough dislocations, resulting in comparable strength compared to CoCrFeNi-1Cu. The addition of Cu in CoCrFeNi was reported to form a Cu-rich fcc phase, suggesting the low solubility of Cu in CoCrFeNi. The *in situ* neutron diffraction analyses and TEM observations suggest that adding more Cu alters the stacking fault formation behavior, which, in turn, alters the deformation mechanism of this alloy system, where twins formation is not necessary to achieve comparable strength. Suppression of twinning has been reported previously in various systems where it is most likely due to the lower energy of deforming in another way, hence twinning not being formed. 52,53

This study has provided a quantitative assessment of many deformation mechanisms in just one HEA system. The noticeable change of microstructure seen from the EDS map and the subsequent deformation mechanism seen from *in situ* tensile measurement by tuning the elemental composition have been revealed. The deformation mechanism of the sample that is observed in this study is similar to other HEAs with the same microstructural features. For example, the CoCrFeNi-1Cu with relatively smaller Cu clusters behaves similarly to CoCrFeMnNi at room temperature where we would see twinning formation at the last stage of deformation. On the other hand, with the existence of relatively larger Cu clusters on CoCrFeNi-3Cu and CoCrFeNi-5Cu, the sample deforms by forming many dislocations, similar to nanoprecipitate-strengthened HEAs.

To summarize, one alloy system was studied where little compositional change led to a plethora of microstructural and mechanistic change, while the macroscopic stress–strain behavior was not changed drastically, observed by both direct and indirect methods which yielded consistent results. *In situ* diffraction and postmortem characterizations were performed on CoCrFeNi-1Cu, CoCrFeNi-3Cu, and CoCrFeNi-5Cu. The ultimate tensile strength, elongation to failure, and stress at necking slightly decreased with increasing Cu content, while yield strength was maintained. Lattice strain evolution shows similar features where softer grain families {220} transfer the load to harder grain families {200}. Stacking fault formation was observed from the difference of lattice strains between {111} and {222} grains in

CoCrFeNi-1Cu at the later stage of deformation. Stacking fault energy calculation on CoCrFeNi-1Cu suggests that twinnings are formed at the later stage of deformation, which was confirmed by the TEM image of post tensile loading sample. Although the lattice strain evolution of CoCrFeNi-3Cu and CoCrFeNi-5Cu did not suggest stacking fault formation, the TEM study shows many dislocations were formed, which causes these alloys to retain their strength and ductility, indicating that twinning alone might not necessarily lead to a high strength.

L.A., Z.L., Y.G., and P.K.L. are grateful for the support from the U. S. National Science Foundation (No. DMR 1809640). Q.D. and H.B. are grateful for the internal funding from the School of Materials Science and Engineering, Zhejiang University. Y.Z. is supported through the Laboratory Directed Research and Development Program at Idaho National Laboratory under the Department of Energy (DOE) Idaho Operations Office (an agency of the U.S. Government) under Contract No. DE-AC07-05ID145142.

AUTHOR DECLARATIONS Conflict of Interest

The authors have no conflicts to disclose.

Author Contributions

Lia Amalia: Data curation (equal); Formal analysis (equal); Investigation (equal); Methodology (equal); Project administration (equal); Resources (equal); Software (equal); Validation (equal); Visualization (equal); Writing – original draft (equal); Writing – review & editing (equal). Yongkang Li: Data curation (equal); Formal analysis (equal); Investigation (equal); Methodology (equal); Resources (equal); Software (equal); Validation (equal); Visualization (equal); Writing – original draft (equal); Writing – review & editing (equal); Formal analysis (equal); Funding acquisition (equal); Investigation (equal); Methodology (equal); Project administration (equal); Resources (equal); Software (equal); Supervision (equal); Validation (equal); Visualization (equal); Writing – original draft (equal); Writing – review & editing (equal). Yan Chen: Data curation

(equal); Formal analysis (equal); Investigation (equal); Methodology (equal); Resources (equal); Software (equal); Validation (equal); Visualization (equal); Writing - original draft (equal); Writing review & editing (equal). Dunji Yu: Data curation (equal); Formal analysis (equal); Investigation (equal); Methodology (equal); Resources (equal); Software (equal); Validation (equal); Visualization (equal); Writing - original draft (equal); Writing - review & editing (equal). Ke An: Data curation (equal); Formal analysis (equal); Investigation (equal); Methodology (equal); Project administration (equal); Resources (equal); Software (equal); Supervision (equal); Validation (equal); Visualization (equal); Writing - original draft (equal); Writing - review & editing (equal). Zongyang Lyu: Data curation (equal); Formal analysis (equal); Investigation (equal); Methodology (equal); Software (equal); Validation (equal); Visualization (equal); Writing - original draft (equal); Writing - review & editing (equal). Peter K. Liaw: Conceptualization (equal); Data curation (equal); Formal analysis (equal); Funding acquisition (equal); Investigation (equal); Methodology (equal); Project administration (equal); Resources (equal); Software (equal); Supervision (equal); Validation (equal); Visualization (equal); Writing - original draft (equal); Writing - review & editing (equal). Yanwen Zhang: Conceptualization (equal); Data curation (equal); Formal analysis (equal); Funding acquisition (equal); Investigation (equal); Methodology (equal); Project administration (equal); Resources (equal); Software (equal); Supervision (equal); Validation (equal); Visualization (equal); Writing - original draft (equal); Writing - review & editing (equal). Qingqing Ding: Conceptualization (equal); Data curation (equal); Formal analysis (equal); Funding acquisition (equal); Investigation (equal); Methodology (equal); Project administration (equal); Resources (equal); Software (equal); Supervision (equal); Validation (equal); Visualization (equal); Writing - original draft (equal); Writing - review & editing (equal). Yanfei Gao: Conceptualization (equal); Data curation (equal); Formal analysis (equal); Funding acquisition (equal); Investigation (equal); Methodology (equal); Project administration (equal); Resources (equal); Software (equal); Supervision (equal); Validation (equal); Visualization (equal); Writing - original draft (equal); Writing - review & editing (equal).

DATA AVAILABILITY

The data that support the findings of this study are available from the corresponding authors upon reasonable request.

REFERENCES

- ¹B. Cantor, I. Chang, P. Knight, and A. Vincent, Mater. Sci. Eng.: A 375-377, 213-218 (2004).
- ²J. W. Yeh, S. K. Chen, S. J. Lin, J. Y. Gan, T. S. Chin, T. T. Shun, C. H. Tsau, and S. Y. Chang, Adv. Eng. Mater. 6(5), 299–303 (2004).
- ³S. Chen, Z. H. Aitken, S. Pattamatta, Z. Wu, Z. G. Yu, D. J. Srolovitz, P. K. Liaw, and Y.-W. Zhang, Mater. Today 65, 14–25 (2023).
- ⁴C. Lee, G. Song, M. C. Gao, R. Feng, P. Chen, J. Brechtl, Y. Chen, K. An, W. Guo, and J. D. Poplawsky, Acta Mater. **160**, 158–172 (2018).
- ⁵Z. Li and D. Raabe, JOM **69**(11), 2099–2106 (2017).
- ⁶J. Su, D. Raabe, and Z. Li, Acta Mater. **163**, 40–54 (2019).
- ⁷L. Liu, Y. Zhang, J. Han, X. Wang, W. Jiang, C.-T. Liu, Z. Zhang, and P. K. Liaw, Adv. Sci. 8(23), 2100870 (2021).
- ⁸Q. Ding, Y. Zhang, X. Chen, X. Fu, D. Chen, S. Chen, L. Gu, F. Wei, H. Bei, Y. Gao, M. Wen, J. Li, Z. Zhang, T. Zhu, R. O. Ritchie, and Q. Yu, Nature 574(7777), 223–227 (2019).

- ⁹Q. Ding, H. Bei, X. Wei, Y. Gao, and Z. Zhang, Mater. Today Nano 14, 100110 (2021).
- ¹⁰ K. H. Lo, C. H. Shek, and J. Lai, Mater. Sci. Eng.: R: Rep. 65(4-6), 39–104 (2009).
- ¹¹G. Laplanche, A. Kostka, O. M. Horst, G. Eggeler, and E. P. George, Acta Mater. 118, 152–163 (2016).
- ¹²Z. Wu, Y. Gao, and H. Bei, Acta Mater. **120**, 108–119 (2016).
- ¹³B. Gwalani, S. Gorsse, V. Soni, M. Carl, N. Ley, J. Smith, A. V. Ayyagari, Y. Zheng, M. Young, R. S. Mishra, and R. Banerjee, Materialia 6, 100282 (2019).
- ¹⁴G. A. Salishchev, M. A. Tikhonovsky, D. G. Shaysultanov, N. D. Stepanov, A. V. Kuznetsov, I. V. Kolodiy, A. S. Tortika, and O. N. Senkov, J. Alloys Compd. 591, 11–21 (2014).
- ¹⁵M. C. Oh, A. Sharma, H. Lee, and B. Ahn, Intermetallics **139**, 107369 (2021).
- ¹⁶Z. G. Zhu, K. H. Ma, Q. Wang, and C. H. Shek, <u>Intermetallics</u> 79, 1–11 (2016).
- ¹⁷J. Lu, B. Wang, X. Qiu, Z. Peng, and M. Ma, Surf. Coat. Technol. 328, 313–318 (2017).
- ¹⁸C.-M. Lin and H.-L. Tsai, J. Alloys Compd. **489**(1), 30–35 (2010).
- ¹⁹L. Jiang, Y. J. Hu, K. Sun, P. Xiu, M. Song, Y. Zhang, W. L. Boldman, M. L. Crespillo, P. D. Rack, and L. Qi, Adv. Mater. 32(39), 2002652 (2020).
- ²⁰B. Kombaiah, Y. Zhou, K. Jin, A. Manzoor, J. D. Poplawsky, J. A. Aguiar, H. Bei, D. S. Aidhy, P. D. Edmondson, and Y. Zhang, ACS Appl. Mater. Interfaces 15(3), 3912–3924 (2023).
- ²¹Y. Zhang, Y. N. Osetsky, and W. J. Weber, Chem. Rev. **122**(1), 789–829 (2021).
- ²²S. Mukanov, P. Loginov, A. Fedotov, M. Bychkova, M. Antonyuk, and E. Levashov, Materials 16(3), 1178 (2023).
- ²³T. G. Lach, C. M. Silva, Y. Zhou, W. L. Boldman, P. D. Rack, W. J. Weber, and Y. Zhang, npj Mater. Degrad. 6(1), 60 (2022).
- ²⁴K. N. Campo, C. C. de Freitas, L. Fanton, and R. Caram, J. Mater. Sci. Technol. 52, 207–217 (2020).
- 25°C. C. de Freitas, R. Caram, and K. N. Campo, Intermetallics 150, 107682 (2022).
- 26_{L. Rogal, Mater. Des. 119}, 406–416 (2017).
- 27 Y. Qi, T. He, and M. Feng, J. Appl. Phys. 129(19), 195104 (2021).
- ²⁸S. Nam, J. Y. Hwang, J. Jeon, J. Park, D. Bae, M. J. Kim, J.-H. Kim, and H. Choi, J. Mater. Res. 34(5), 720–731 (2019).
- ²⁹S. San, Y. Tong, H. Bei, B. Kombaiah, Y. Zhang, and W.-Y. Ching, Mater. Des. 209, 110071 (2021).
- 30 K. An, Y. Chen, and A. D. Stoica, MRS Bull. 44(11), 878-885 (2019).
- ³¹K. An, H. D. Skorpenske, A. D. Stoica, D. Ma, X.-L. Wang, and E. Cakmak, Metall. Mater. Trans. A 42(1), 95–99 (2011).
- ³²K. An, ORNL Report No. ORNL-TM-2012-621 (2012).
- ³³M. Frank, Y. Chen, S. Nene, S. Sinha, K. Liu, K. An, and R. Mishra, Mater. Today Commun. 23, 100858 (2020).
- ³⁴W. Woo, J. S. Jeong, D. K. Kim, C. M. Lee, S. H. Choi, J. Y. Suh, S. Y. Lee, S. Harjo, and T. Kawasaki, Sci. Rep. 10(1), 1350 (2020).
- 35Z. Wang, A. D. Stoica, D. Ma, and A. M. Beese, Mater. Sci. Eng.: A 674, 406–412 (2016).
- 36S. Harjo, Y. Tomota, P. Lukáš, D. Neov, M. Vrana, P. Mikula, and M. Ono, Acta Mater. 49(13), 2471–2479 (2001).
- 37 T. Ungár, I. Dragomir, Á. Révész, and A. Borbély, J. Appl. Crystallogr. 32(5),
- 992-1002 (1999).

 38W Woo T Ungár 7 Feng F Kenik and R Clausen Metall Mater Trans
- ³⁸W. Woo, T. Ungár, Z. Feng, E. Kenik, and B. Clausen, Metall. Mater. Trans. A 41, 1210–1216 (2010).
- ³⁹A. Borbély, J. Dragomir-Cernatescu, G. Ribárik, and T. Ungár, J. Appl. Crystallogr. 36(1), 160–162 (2003).
- ⁴⁰W. Woo, M. Naeem, J.-S. Jeong, C.-M. Lee, S. Harjo, T. Kawasaki, H. He, and X.-L. Wang, Mater. Sci. Eng.: A 781, 139224 (2020).
- ⁴¹W. Zhang, Y. Gao, Z. Feng, X. Wang, S. Zhang, L. Huang, Z. Huang, and L. Jiang, Acta Mater. **194**, 378–386 (2020).
- ⁴²R. Blondé, E. Jimenez-Melero, L. Zhao, J. Wright, E. Brück, S. Van der Zwaag, and N. Van Dijk, Acta Mater. 60(2), 565–577 (2012).
- 43B. Cai, B. Liu, S. Kabra, Y. Wang, K. Yan, P. D. Lee, and Y. Liu, Acta Mater. 127, 471–480 (2017).
- ⁴⁴K. Yan, K.-D. Liss, I. B. Timokhina, and E. V. Pereloma, Mater. Sci. Eng.: A 662, 185–197 (2016).
- 45Y. Wang, B. Liu, K. Yan, M. Wang, S. Kabra, Y.-L. Chiu, D. Dye, P. D. Lee, Y. Liu, and B. Cai, Acta Mater. 154, 79–89 (2018).

- ⁴⁶M. Frank, S. S. Nene, Y. Chen, B. Gwalani, E. J. Kautz, A. Devaraj, K. An, and R. S. Mishra, Sci. Rep. 10(1), 22263 (2020).
- ⁴⁷K. Yamanaka, M. Mori, S. Sato, and A. Chiba, Sci. Rep. 7(1), 10808 (2017).
- 48 M. Frank, S. S. Nene, Y. Chen, S. Thapliyal, S. Shukla, K. Liu, S. Sinha, T. Wang, M. J. Frost, K. An, and R. S. Mishra, Appl. Phys. Lett. 119(8), 081906 (2021)
- 49 L. Fan, T. Yang, Y. Zhao, J. Luan, G. Zhou, H. Wang, Z. Jiao, and C.-T. Liu, Nat. Commun. 11(1), 6240 (2020).
- ⁵⁰W. Wu, M. Song, S. Ni, J. Wang, Y. Liu, B. Liu, and X. Liao, Sci. Rep. 7(1), 46720 (2017).
- 51A. Verma, P. Tarate, A. C. Abhyankar, M. R. Mohape, D. S. Gowtam, V. P. Deshmukh, and T. Shanmugasundaram, Scr. Mater. 161, 28–31 (2019).
- ⁵²M. Vronka, M. Karlik, J. Vesely, J. Manak, and O. Heczko, J. Mater. Sci. 54(8), 6586–6593 (2019).
- 53S. Stappert, B. Rellinghaus, M. Acet, and E. Wassermann, Eur. Phys. J. D-At., Mol., Opt. Plasma Phys. 24, 351–354 (2003).
- 54K. Ming, X. Bi, and J. Wang, Int. J. Plasticity 100, 177–191 (2018).